

See discussions, stats, and author profiles for this publication at: <https://www.researchgate.net/publication/45581950>

Kinetic Reaction Modeling Framework for Identifying and Quantifying Reductant Reactivity in Heterogeneous Aquifer Sediments

ARTICLE *in* ENVIRONMENTAL SCIENCE & TECHNOLOGY · SEPTEMBER 2010

Impact Factor: 5.33 · DOI: 10.1021/es101661u · Source: PubMed

CITATIONS

13

READS

53

5 AUTHORS, INCLUDING:



Henning Prommer

University of Western Australia / CSIRO Lan...

112 PUBLICATIONS 1,896 CITATIONS

SEE PROFILE



Carolyn E. Oldham

University of Western Australia

66 PUBLICATIONS 653 CITATIONS

SEE PROFILE



Niels Hartog

KWR Watercycle Research Institute

46 PUBLICATIONS 274 CITATIONS

SEE PROFILE

Kinetic Reaction Modeling Framework for Identifying and Quantifying Reductant Reactivity in Heterogeneous Aquifer Sediments

CARLOS DESCOURVIERES,^{*,†,‡}
HENNING PROMMER,^{‡,§}
CAROLYN OLDHAM,[†]
JANEK GRESKOWIAK,[‡] AND
NIELS HARTOG^{||}

School of Environmental Systems Engineering, The University of Western Australia, Crawley 6009, Australia, CSIRO Land and Water, Floreat, Western Australia 6913, Australia, School of Earth and Environment, The University of Western Australia, Crawley 6009, Australia, and Deltares, Soil and Groundwater Systems, Utrecht, The Netherlands

Received May 15, 2010. Revised manuscript received July 20, 2010. Accepted July 20, 2010.

Water-sediment interactions triggered by the injection of oxidized aqueous solutions into anoxic groundwater systems usually modify both the aquifer matrix and control the final aqueous composition. The identification and quantification of these reactions in complex heterogeneous systems remains a challenge for the analysis and prediction of water quality changes. Driven by the proposed injection of large quantities of oxic water into a deep anoxic heterogeneous pyritic aquifer; this study was undertaken to quantify the reactivity of aquifer sediments with respect to oxidant consumption and to characterize the variability of the reaction rates across different lithological units. A total of 53 samples were incubated for periods of 14, 37, and 50 days, during which the gas-phase was continuously monitored and the aqueous composition analyzed. A geochemical modeling framework was developed that incorporated a mixed set of equilibrium and kinetic reactions and supported the interpretation and quantification of the geochemical controls. The good agreement between simulated and experimental results of O₂ consumption, CO₂ production, pH, major ions, and trace metals suggests that the framework was able to successfully quantify reaction rates of competing redox and buffering reactions for the different lithological aquifer material.

Introduction

The injection of oxidizing aqueous solutions into anoxic groundwater systems triggers a series of geochemical reactions that modify both the aquifer matrix and the injectant

composition. This scenario is usually encountered during (i) the application of subsurface remediation techniques aimed at promoting oxidative degradation of contaminants such as petroleum hydrocarbons and polycyclic aromatic hydrocarbons (1, 2), (ii) *in situ* leaching of minerals (3), and (iii) water reuse techniques, particularly aquifer storage and recovery (ASR) and deepwell injection (4, 5). In all these cases, *a priori* understanding of the anticipated geochemical zonation is required to predict and eliminate potential operational (clogging, mineral dissolution) as well as environmental risks such as the mobilization of trace metals. The injection of reclaimed water typically cause changing geochemical conditions, especially pH and redox zonation. These conditions may have a significant impact on the fate of residual trace organics and on the degree of trace metal mobilization and their potential for subsequent attenuation. Understanding the fate of redox-sensitive species therefore relies on the identification and adequate quantification of the dominating redox and buffering processes (6, 7).

Earlier investigations on the reactivity of anoxic aquifers have repeatedly shown the importance of pyrite and sedimentary organic matter (SOM) as reductants (8, 9). Pyrite oxidation kinetics have been extensively studied in the laboratory under unsaturated and saturated conditions (10, 11), and methods applied to determine pyrite oxidation rates include monitoring of dissolved sulfate over time (12, 13), or monitoring of gas composition in sealed environments (14). For natural sediments, these methods alone may provide insufficient constraints as multiple reductants (e.g., pyrite, SOM, Fe(II)-aluminosilicates, and Fe(II)-carbonates) compete for the introduced oxidants (15). In heterogeneous aquifers the importance of a particular reaction may strongly vary depending on the composition of individual lithological units. While physical (hydrogeological) heterogeneity controls the extent of the contact between the injected water and specific lithological units, and its effect on solute transport and water quality evolution has been widely studied (16, 17), heterogeneity in aquifer reactivity (chemical heterogeneity) is rarely accounted for in a comprehensive manner (18, 19).

We use a combined methodology, incorporating numerical modeling, previously described incubation data (8), and new experimental kinetic data, to understand the impact of chemical heterogeneity on the dominant redox and buffering processes. We use this approach specifically to (i) quantify the reaction kinetics toward oxygen of individual reductants and secondary reactions and (ii) efficiently characterize the spatial and temporal variability of reaction rates in different lithologies of an anoxic, physically and chemically heterogeneous aquifer.

Materials and Methods

Sediment Sampling and Characterization. Sediment samples were recovered 190–530 m below ground level (mbgl) from two separate boreholes through the sedimentary sequence of the Leederville aquifer north of Perth (M345 and BY07, Figure S1). Drill cores were split in a specifically designed anoxic N₂-positive pressure chamber installed next to the drilling rig. Samples were stored in sealed containers under N₂ atmosphere below 4 °C to prevent oxidation until experiments commenced. The aquifer material comprised a sequence of sands, silts, and clays. Bulk sediment samples were analyzed (cf. SI) for major and trace elements, pyrite, total carbon (TC), total organic carbon (TOC), total inorganic carbon (TIC), and cation exchange capacity (CEC).

Incubation Experiments. Eighteen samples from borehole BY07 were incubated in addition to 27 samples from borehole

* Corresponding author phone: +61 8 9333 6272; fax: +61 8 9333 6211; e-mail: carlos.descourvieres@csiro.au. Corresponding author address: School of Environmental Systems Engineering, The University of Western Australia, M015, 35 Stirling Hwy, Crawley, WA 6009.

[†] School of Environmental Systems Engineering, The University of Western Australia.

[‡] CSIRO Land and Water.

[§] The University of Western Australia.

^{||} Deltares, Soil and Groundwater Systems.

M345 (8). The samples represented the stratigraphic heterogeneity of the three predominant lithologies (sand, silt, and clay). They were split into duplicates, and the sediment (22.5 g) was mixed with 130 mL of ultrapure anoxic water in 250-mL Duran bottles under a N₂-atmosphere, leaving a constant headspace. Samples were incubated at 24.2 ± 1 °C and connected for 50 days to an indirect closed circuit respirometer (Micro-Oxymax). During this period O₂ consumed and CO₂ produced were measured consecutively in each bottle, resulting in measurements every 2.7 h for each incubation. The sediment-water slurry was magnet-stirred at 200 rpm to ensure a homogeneous chemical system and enhance oxygen diffusion from the head space to the aqueous phase. Before and after incubation, pH and Eh were measured using a hand-held meter. Once experiments were finished, the sediment slurries were centrifuged, and the filtered supernatants (0.45 μm) were analyzed for major and minor ions.

Additional sacrificial incubations of selected samples were performed to determine the change in the chemical composition of the aqueous solutions. The 74 nonsacrificial replicate experiments showed little variability in final chemical composition and gas phase evolution; we therefore assumed that the observations during sacrificial experiments were representative. Four sediment samples from bore BY07 (Table 2) were divided into ten subsamples and one reference sample and connected to the respirometer as previously described. For samples B13 and B26, subsamples were sequentially removed from the respirometer after 0, 1, 2, 3, 4, 5, 6, 8, 10, 12, days and the reference sample disconnected after 14 days. For samples B19 and B23, subsamples were removed after 0, 1, 4, 7, 11, 14, 18, 23, 28, and 32 days, and the reference sample was disconnected after 37 days. At each sampling time, a volume of 2.5 mL was collected from the reference sample and analyzed for Na⁺, K⁺, Ca²⁺, Mg²⁺, Cl⁻, SO₄²⁻ by ion-chromatography, pH and Eh. The removed volume was replaced by anoxic ultrapure water to maintain a constant headspace. For each removed subsample, supernatants were analyzed as *per* the initial incubation experiments.

Geochemical Modeling Framework. PHREEQC-2 (20) was used to define and quantify the reactive processes that controlled both aqueous and sediment chemistry during the experiments. The process selection relied on semiquantitative results from sediment samples from core M345 (8) and were used to define the set of geochemical reactions to explain the measured O₂ consumption, CO₂ production and final supernatant composition. The temporal evolution of concentrations, as dictated by the interaction between the various oxidation and buffering reactions, and the partitioning between the aqueous and gas phases, was simulated through a combination of equilibrium and kinetic reactions with rate expressions compiled from the literature, e.g., ref 21.

Definition of Initial Conditions. At the onset of the incubation experiments, when ultrapure anoxic water and a well-characterized sediment sample were brought into contact, mass exchange between the aqueous solution and the headspace occurred through equilibration of aqueous CO₂ and O₂ concentrations. The interaction between the deionized water and sediments likely caused an alteration of the ion exchange site occupation. Therefore, this initial phase was simulated by (i) defining the initial concentrations of each mineral in the sediments according to the measured concentrations (Table 1), (ii) assuming that the ion exchange sites associated with the sediments were in equilibrium with the average ambient groundwater composition at the measured CEC (Table 1), and (iii) assuming initial gas equilibrium at atmospheric pressures for O₂ (10^{-0.67} atm) and CO₂ (10^{-3.5} atm).

Mineral Reaction Kinetics. The oxidation reactions induced by the availability of molecular oxygen together with the associated pH-buffering reactions were expected to be the key

TABLE 1. Initial Sediment Parameters Included in the Kinetic Model^a

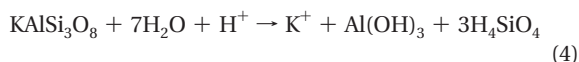
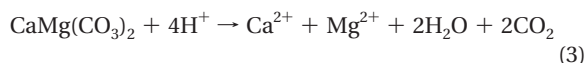
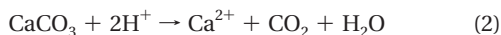
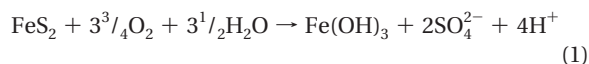
lithology/sample	quartz w/w%	K-feldspar w/w%	albite w/w%	pyrite w/w%	glauconite w/w%	kaolinite w/w%	calcite w/w%	siderite w/w%	ankerite w/w%	TOC w/w%	CEC meq/100 g
sand (n = 124)	64.1 ± 10	26.6 ± 5.8	2.05 ± 2.3	0.60 ± 0.9	0.04 ± 0.4	5.85 ± 4.8	0.01 ± 0.05	0.12 ± 0.6	0.06 ± 0.6	0.52 ± 0.8	2.62 ± 2.1
silt (n = 43)	39.6 ± 11	29.4 ± 5.6	2.67 ± 1.9	1.54 ± 1.4	nd	24.2 ± 10	0.02 ± 0.01	0.77 ± 2.3	nd	1.63 ± 1.2	7.60 ± 4.7
clay (n = 25)	17.8 ± 13	20.4 ± 5.4	0.87 ± 0.9	2.45 ± 2.2	nd	54.3 ± 14	0.006 ± 0.007	0.87 ± 1.5	nd	3.86 ± 3.5	11.8 ± 6.1
BR13	54.0	28.0	nd	0.07	nd	15.0	nd	nd	nd	0.77	4.00
BR19	64.0	29.0	1.00	1.23	nd	4.00	nd	nd	0.14	0.23	2.00
BR23	58.0	29.0	0.20	0.96	nd	9.00	0.016	nd	0.11	0.12	2.00
BR26	31.0	30.0	4.00	0.37	nd	28.0	0.015	1.50	1.61	2.37	8.00

^a nd: not determined.

TABLE 2. Estimated Average Parameter Values Used in the Calibrated Models

trace metal	trace metals stoichiometric release ratio (Y_{met} , mol/mol FeS_2 dissolved)			
	elemental analysis (XRF)	optimized average ratio		
Ni	5×10^{-4}	9.1×10^{-4}		
Cu	5×10^{-4}	7.0×10^{-4}		
Mn	6×10^{-3}	6.9×10^{-3}		
Pb	1×10^{-4}	5.7×10^{-4}		
Cd	4×10^{-5}	2.0×10^{-5}		
Zn	1×10^{-4}	7.2×10^{-3}		
Co	1×10^{-4}	3.5×10^{-4}		
A_{mineral}/V (m^2/L)	sand	silt	clay	source
pyrite	$1.9 \pm 1.7 \times 10^{-1}$	$7.0 \pm 4.7 \times 10^{-1}$	1.0 ± 0.3	model calibration
K-feldspar	$3.3 \pm 1.6 \times 10^3$	$9.9 \pm 3.3 \times 10^2$	$6.0 \pm 3.0 \times 10^2$	model calibration
albite	$4.3 \pm 1.2 \times 10^2$	$6.6 \pm 1.7 \times 10^2$	$3.5 \pm 0.4 \times 10^2$	model calibration
calcite	$1.1 \pm 0.7 \times 10^{-1}$	$4.4 \pm 3.3 \times 10^{-2}$	$4.0 \pm 1.0 \times 10^{-4}$	model calibration
ankerite	1.6 ± 0.7	$7.1 \pm 5.3 \times 10^{-1}$	$1.3 \pm 0.2 \times 10^{-1}$	model calibration
k_k (eq 10, $\text{mol}/\text{m}^2/\text{s}$)				
$\text{Al}(\text{OH})_3$	$2.0 \pm 1.3 \times 10^{-12}$	$2.6 \pm 1.1 \times 10^{-12}$	$5.1 \pm 4.9 \times 10^{-13}$	model calibration
$\text{Fe}(\text{OH})_3$	$1.2 \pm 0.7 \times 10^{-11}$	$4.3 \pm 3 \times 10^{-11}$	$2.0 \pm 1.8 \times 10^{-14}$	model calibration
k_{O_2} (eq 12, $\text{mol}/\text{L}/\text{s}$)				
SOM	1.57×10^{-9}	1.57×10^{-9}	1.57×10^{-9}	20

drivers for the changes in the aqueous composition. Pyrite oxidation was the main sink of O_2 (8), and the resulting acidification was the driver for the release of major ions and trace metals into solution (eq 1). The release of protons was first buffered by the rapid dissolution of trace level carbonates (eq 2), followed by dissolution of ankerite/dolomite (eq 3), and feldspars (eq 4). The representing sequence of reactions was



The pyrite content in the sediments varied from trace concentrations in very clean sands up to 2.4 wt % in clays (Table 1), and its oxidation by molecular oxygen was included in the reaction network based on the previously applied rate expression (10, 22)

$$r_{\text{pyr}} = 10^{-10.19} C_{\text{O}_2}^{0.5} C_{\text{H}^+} - 0.11 \left(\frac{A_{\text{pyr}}}{V} \right) \left(\frac{C}{C_0} \right)_{\text{pyr}}^{0.67} \left(1 - \left(\frac{\text{IAP}}{K} \right) \right)_{\text{pyr}} \quad (5)$$

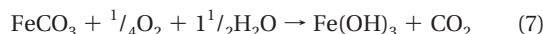
where r_{pyr} is the reaction rate for pyrite ($\text{mol}/\text{L}/\text{s}$), and C_{O_2} and C_{H^+} are the aqueous dissolved oxygen (DO) and proton concentrations. The term (A_{pyr}/V) is the ratio of mineral surface area to solution volume, (C/C_0) is a factor to account for changes in A resulting from the successively progressing reaction (23), and (IAP/K) is the saturation ratio.

The acid buffering dissolution of easily dissolvable carbonate with subsequent release of CO_2 to the head space was included in the reaction network using calcite. The selected rate expression was applicable for both dissolution and precipitation (24, 25)

$$r_{\text{calcite}} = (k_1[\text{H}^+] + k_2[\text{CO}_2] + k_3[\text{H}_2\text{O}] - k_4[\text{Ca}^{2+}][\text{HCO}_3^-]) \left(\frac{A_{\text{calcite}}}{V} \right) \left(\frac{C}{C_0} \right)_{\text{calcite}}^{0.67} \quad (6)$$

where brackets indicate activities. The coefficients k_1 – k_4 are rate constants dependent on temperature, calculated from

experimental data and corrected for the experimental temperature, see the SI. Other Fe(II)-carbonates phases identified, such as ankerite and siderite, also competed for oxygen and contributed to CO_2 production as



Siderite and ankerite were respectively included in the model as FeCO_3 with $\log K = -10.89$ (20), and $\text{CaFe}_{0.6}\text{Mg}_{0.4}(\text{CO}_3)_2$ (26) with $\log K = -17.40$ (27). The dissolution rate expressions for ankerite and siderite were simulated as (25)

$$r_{\text{Fe(II)-carbonates}} = (2.6 \times 10^{-7} [\text{H}^+]^n + 10^{-8} [\text{CO}_2]^n + 2.2 \times 10^{-12}) \times \left(\frac{A_{\text{Fe(II)-carbonates}}}{V} \right) \left(\frac{C}{C_0} \right)_{\text{Fe(II)-carbonates}}^{0.67} \left(1 - \left(\frac{\text{IAP}}{K} \right) \right)_{\text{Fe(II)-carbonates}} \quad (8)$$

with $n = 0.50$ – 0.75 (25, 28). We used the average value of $n = 0.65$.

The weathering of aluminosilicates, mainly K-feldspars (KAlSi_3O_8) and albite ($\text{NaAlSi}_3\text{O}_8$) minerals was described by the generalized equation (29)

$$r_{\text{al-sil}} = \left(k_{\text{H}^+} \frac{[\text{H}^+]^n}{f_{\text{H}}} + k_{\text{H}_2\text{O}} \frac{1}{f_{\text{H}_2\text{O}}} + k_{\text{OH}^-} \frac{[\text{OH}^-]^o}{f_{\text{OH}}} + k_{\text{CO}_2} \frac{[\text{CO}_2]^{0.6}}{f_{\text{CO}_2}} \right) \times \left(\frac{A_{\text{al-sil}}}{V} \right) \left(\frac{C}{C_0} \right)_{\text{al-sil}}^{0.67} \left(1 - \left(\frac{\text{IAP}}{K} \right) \right)_{\text{al-sil}} \quad (9)$$

where $r_{\text{al-sil}}$ is the reaction rate ($\text{mol}/\text{m}^2/\text{s}$), k_i are the rate coefficients for the solutes that influence the rate ($\text{mol}/\text{m}^2/\text{s}$), $[i]$ indicates the solute activities of H^+ , OH^- , and the partial pressure of CO_2 , n and o are the apparent reaction orders, and f_i are inhibition factors by solution elements. The implemented rate coefficients (k_i) were recalculated for the experimental temperature using the Arrhenius equation from tabulated coefficients at 8 °C, along with proposed values (29) for n , o , and f_i in the model (see the SI).

During the incubation experiments, Fe- and Al-oxides precipitation and dissolution were assumed to be kinetically

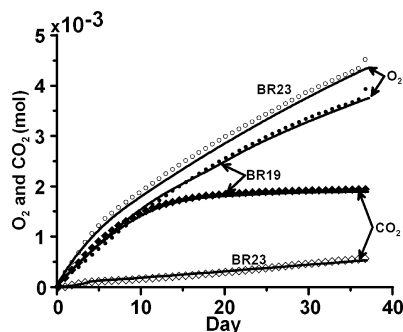


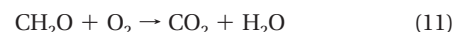
FIGURE 1. Selected cumulative O_2 consumption and CO_2 production during incubation of the reference sample during sacrificial experiments: experimental results (symbols) and simulated model results (solid lines). Samples BR13 and BR26 are presented in Figure S3.

controlled. Reaction rate laws for these minerals were defined as (30)

$$r_k = k_k \left(1 - \left(\frac{IAP}{K} \right) \right)_k \quad (10)$$

where k_k is an empirical constant.

Organic Matter Degradation. During incubations, aerobic SOM oxidation (represented as carbohydrate and based on TOC concentrations) contributed to a variable O_2 consumption and accumulation of CO_2 in the headspace:



Kinetic reactions were formulated for the oxidation of SOM based on the Monod-type rate expression (20)

$$r_{SOM} = k_{O_2} \frac{C_{O_2}}{2.94 \times 10^{-4} + C_{O_2}} \quad (12)$$

where r_{SOM} is the SOM degradation rate, C_{O_2} is the DO concentrations, and k_{O_2} is the rate constant.

Trace Metal Release and Sorption. Acidification produced by pyrite oxidation was accompanied by the release of trace metals such as Ni, Zn, Co, Pb, Mn, and Cu by primary and secondary mineral dissolution. Once released, trace metals may remain in solution, adsorb onto exchange sites, or onto the surface of neo-formed hydrous ferric oxides (HFO) (eq 1), depending on the aqueous composition, in particular pH and HFO concentrations. A stoichiometric ratio (Y_{met}) of the trace metals relative to the sediment pyrite content was

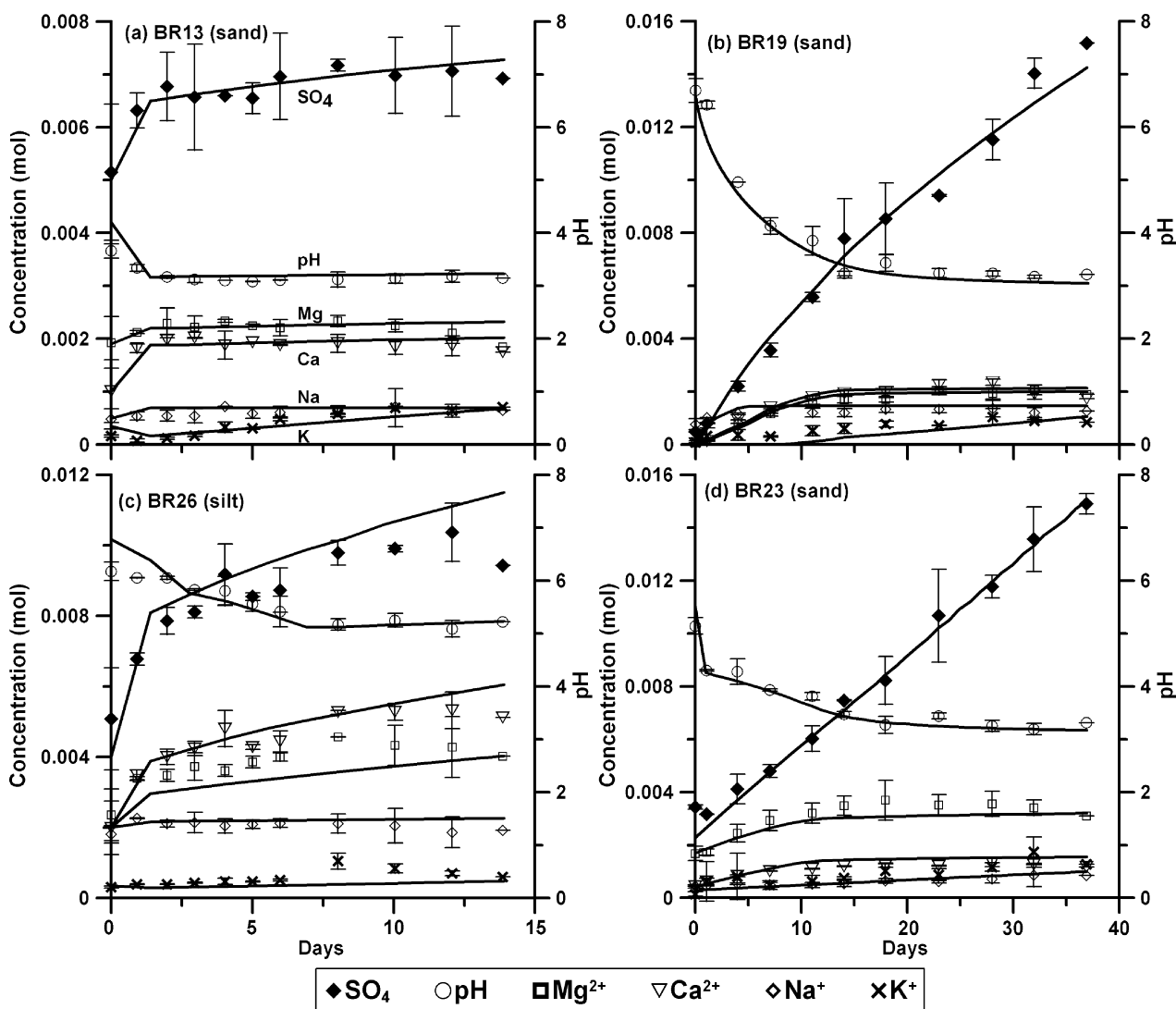


FIGURE 2. Average measured (symbols) and simulated (solid lines) supernatant ion concentrations and pH over 14 days in samples (a) BR13 and (b) BR26 and over 37 days in samples (c) BR19 and (d) BR23. Error bars represent the variation between sacrificed and reference incubation batches.

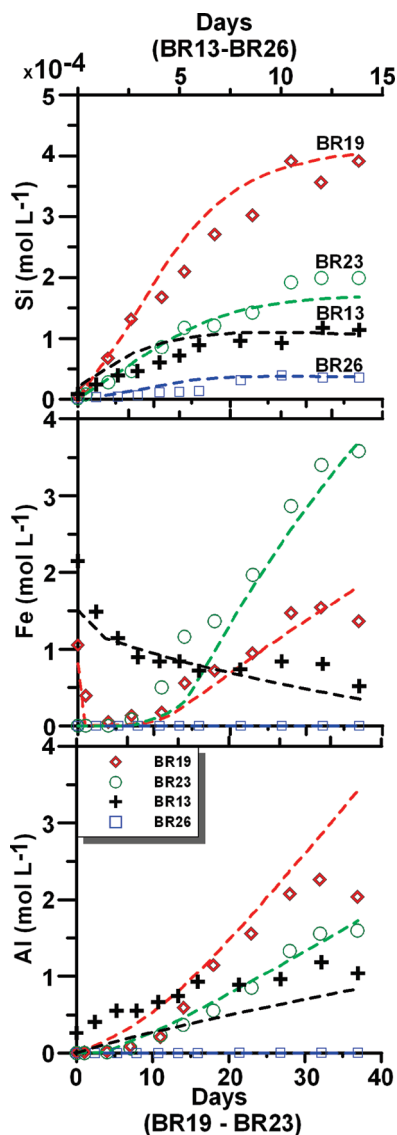


FIGURE 3. Experimental (symbols) and simulated (dashed lines) aqueous concentrations. (a) Si, (b) Fe, and (c) Al in samples BR13, BR19, BR23, and BR26.

determined (Table 2) using correlation analyses assuming that pyrite was the major iron source (8). Thus a trace metal release rate (r_{met}) was defined from the stoichiometric ratio (Y_{met}) and the pyrite oxidation rate (r_{pyr}) by $r_{met} = Y_{met} \times r_{pyr}$. Trace metal sorption was considered through cation exchange reactions and surface complexation. A generalized two-layer surface complexation model was employed with the properties of the newly precipitated HFO as proposed by Dzombak and Morel (31) i.e., weak and strong site densities of 0.2 and 0.005 mol/mol of ferrihydrite respectively and surface area of 600 m²/g.

Reaction Model Calibration. The reaction model comprised a series of interdependent kinetic reactions with initially unknown reaction rate parameters. As the mineral surface areas were not known, the terms (A/V) for each mineral were subject to a stepwise calibration, along with rate constants for Al- and Fe-hydroxides and SOM. Initially, a manual calibration was carried out in PHREEQC-2 for the parameters controlling pyrite, SOM, carbonate, and feldspar dissolution, using the aqueous SO_4^{2-} , Ca^{2+} , Mg^{2+} , K^+ , and Na^+ concentrations, pH, and measured O_2 consumption and CO_2 production as constraints. Subsequently, model parameters were optimized coupling PHREEQC-2 to the nonlinear parameter estimation inversion code PEST (32).

Results and Discussion

Gas-Phase Evolution. The nonsacrificial incubation experiments showed varying O_2 consumption and CO_2 production across the different lithologies. O_2 consumption was up to 1 order of magnitude higher than CO_2 production, with consumption and production generally lower for sands than clays (8). The gas-phase evolution during the sacrificial experiments showed low CO_2 production, reflecting the limited carbonate-associated pH-buffering capacity and low SOM reactivity, e.g. sample BR23 (Figure 1). Analytical results suggested the presence of <0.06% highly reactive carbonates which was in agreement with model-based estimates of <0.1 wt % (8). Similarly, the decreasing CO_2 production of sample BR19 indicated the depletion of the buffering capacity, showing that dissolution of less reactive carbonates and SOM oxidation were responsible for the longer-term production of CO_2 (i.e., >5 days). The reaction network constrained by the monitored O_2 and CO_2 evolution suggested the contribution of SOM to oxygen consumption was less prominent despite SOM being more abundant than pyrite. This suggests a refractory nature of SOM, contributing to persistent elevated sulfate concentrations in the field. The model results closely described both the O_2 consumption and CO_2 production (Figure 1; cf. the SI for nonsacrificial incubation results).

Changes in Supernatant Composition. Changes in dissolved major ion composition were mainly controlled by mineral dissolution. For the incubated sediments, the simulated final and temporal major-ion concentrations and pH showed overall an excellent agreement with the observations (cf. the SI). Ion concentrations were highest in samples that showed a low final pH and high SO_4 concentrations. Observed sulfate concentrations correlated negatively with pH ($R^2 = 0.87$) in the nonsacrificial experiments, confirming that the acidification triggered by pyrite oxidation was the driving mineral dissolution process. The sacrificial experiments BR13, BR23, and BR26 demonstrated a rapid initial increase in Ca, Mg, and SO_4 concentrations and a rapid pH decrease upon contact of the sediments with ultrapure water (Figure 2). In contrast to the nonsacrificial incubations, SEM images of neo-precipitated gypsum ($CaSO_4 \cdot H_2O$) and epsomite ($MgSO_4 \cdot 7(H_2O)$) on some of the sediment material used in the sacrificial experiments suggested that the sediments were affected by pyrite oxidation during storage. Therefore, the observed change in pH from 6.5 to ~4–5 seen in the first data point (day zero) of samples BR13 and BR23, respectively, can be attributed to the accumulation of acidity during premature oxidative dissolution of pyrite. Rapid dissolution of gypsum and epsomite precipitated during storage caused the nonzero Ca, Mg, and SO_4 concentrations in the first supernatant sample (Figure 2). To account for this in the model, we released acidity (by pyrite dissolution) and dissolved gypsum and epsomite to match the initial pH, Ca, Mg, and SO_4 concentrations. With time, sulfate concentrations continued to increase due to pyrite oxidation. Ca and Mg concentrations increased during the first days of incubation as remaining carbonates acted as pH-buffers. The rapid depletion of the carbonates indicated the limited buffering capacity of samples BR13, BR19, and BR23. No further increase in Ca and Mg concentrations occurred after CO_2 production ceased, indicating that carbonate dissolution was their sole source. Following carbonate depletion, feldspar and minor plagioclase dissolution continued to buffer pH at lower levels (~3), accompanied by an increase in aqueous K (Figure 2) and Al and Si (Figure 3). Sample BR26 contained a relatively higher carbonate buffering capacity, and therefore the pH values did not decrease below 5. The observed initial increase in Na concentrations was mainly attributed to the initial re-equilibration of the exchanger composition. The Na concentrations therefore depended mostly on the pH and prevailing Ca and Mg concentrations.

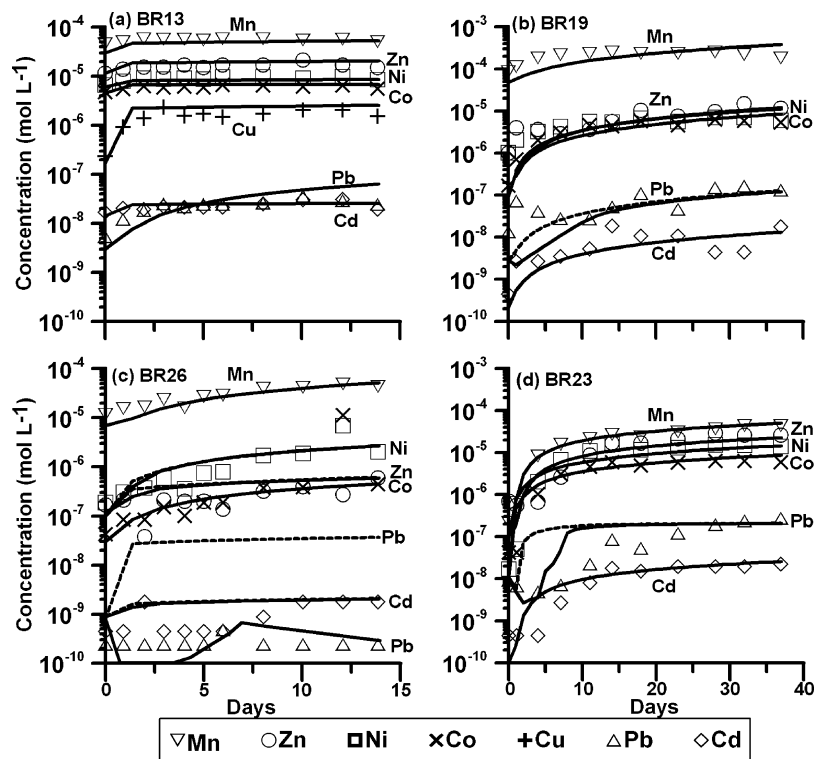


FIGURE 4. Experimental (symbols) and simulated (solid lines) aqueous trace metal concentrations for sacrificial incubation experiments: (a) BR13 (sand), (b) BR19 (sand), (c) BR26 (silt), and (d) BR23 (sand). Dashed lines represent simulated results without surface complexation reactions.

Mineral Precipitation and Its Impact on Trace Metal Concentrations. In the pH range 4–6 the supernatant solutions exhibited very low aqueous Fe and Al concentrations. The model simulations illustrated that within this pH range Fe and Al concentrations were indeed controlled by the solubility of $\text{Fe}(\text{OH})_3$ and $\text{Al}(\text{OH})_3$ precipitated during the simulations. Aqueous Fe and Al concentrations increased linearly when $\text{pH} < 4$ and alkalinity declined (Figure 3) due to the (re)dissolution of $\text{Al}(\text{OH})_3$ and $\text{Fe}(\text{OH})_3$. Simulations indicated that dissolved Si was derived from aluminosilicates dissolution. Where saturation was reached, equilibrium precipitation of (amorphous) SiO_2 was allowed to occur. For the sacrificial incubations the comparison between simulated and observed Al, Fe, and Si concentrations are shown in Figure 3.

Supernatant concentrations of selected trace metals increased with decreasing pH and increasing SO_4^{2-} concentrations in both the sacrificial (Figure 4), and nonsacrificial incubations (cf. the SI). A sharp increase in concentrations occurred when pH decreased below 4, which coincided with the depletion in alkalinity and near saturation conditions for ferric oxyhydroxides (Figures 2 and 4). The model closely described the observed concentrations (Figure 4). The simulation results indicated that sorption by surface complexation exerted a major control in aqueous metal concentrations at circumneutral pH. Ion exchange, however, was found to be of minor importance. Trace metal concentrations were dependent on the pH-dependent abundance of sorption sites provided by ferrihydrite. This was influenced by the low quantity of sorption sites created at the beginning of the experiments due to the low amount of pyrite dissolved. The sorption control was most evident for Pb, where the results for samples BR-19 and BR23 indicated that surface complexation limited aqueous concentrations during the first days of the incubation period. In contrast, for incubation BR26, higher pH and surface complexation to HFOs controlled Pb concentrations.

Optimized Reaction Rate Parameters. The optimized rate parameters for the incorporated mineral reactions were classified using the sample's lithology (Table 2). In general, the optimized (A/V) values differed clearly between the two lithological end members (sand and clay). The values determined for the silts overlapped the range defined by sands and clays. Average (A/V) values determined for pyrite reflected higher concentrations/surface area in the finer sediments. An opposite trend was observed for aluminosilicates and carbonates, where optimized (A/V) values were highest in the sands, reflecting their higher concentrations.

The average concentration-normalized pyrite weathering rates over the first 5 days were within the range of previously reported pyrite (monomineralic) oxidation rates determined in the laboratory at circumneutral pH and 25 °C (10, 11, 14, 33). The pyrite concentration-normalized weathering rates across lithologies (Figure 5) were within similar orders of magnitude indicating that pyrite mineral size was similar across the different lithologies. Estimated (A/V) values (Table 2) and average pyrite concentrations (Table 1) used per incubation suggest specific surface areas of 0.1 and 0.2 $\text{m}^2 \text{g}^{-1}$ for the sands and clays, respectively. These areal estimates are slightly higher than the reported pyrite surface area of 0.07 $\text{m}^2 \text{g}^{-1}$ (11) and lower than reported for framboidal pyrite of 0.77 $\text{m}^2 \text{g}^{-1}$ (34). Specific aluminosilicates surface areas ranged from 13 to 50 $\text{m}^2 \text{g}^{-1}$ for K-feldspars and 90 to 178 $\text{m}^2 \text{g}^{-1}$ for albite. Carbonate reactive surface areas ranged from 0.5 to 0.002 $\text{m}^2 \text{g}^{-1}$ for calcite and 7 to 0.07 $\text{m}^2 \text{g}^{-1}$ for ankerite, in agreement with determined biogenic calcite surface areas (35).

The concentration-normalized aluminosilicate and carbonate weathering rates were 1 order of magnitude higher than for pure mineral phases reported in the literature. This was due to the pyrite oxidation rate and consequent acid production actively controlling the subsequent mineral dissolution rate. Despite the discrepancy in absolute values, the model-derived rates corresponded with reported dif-

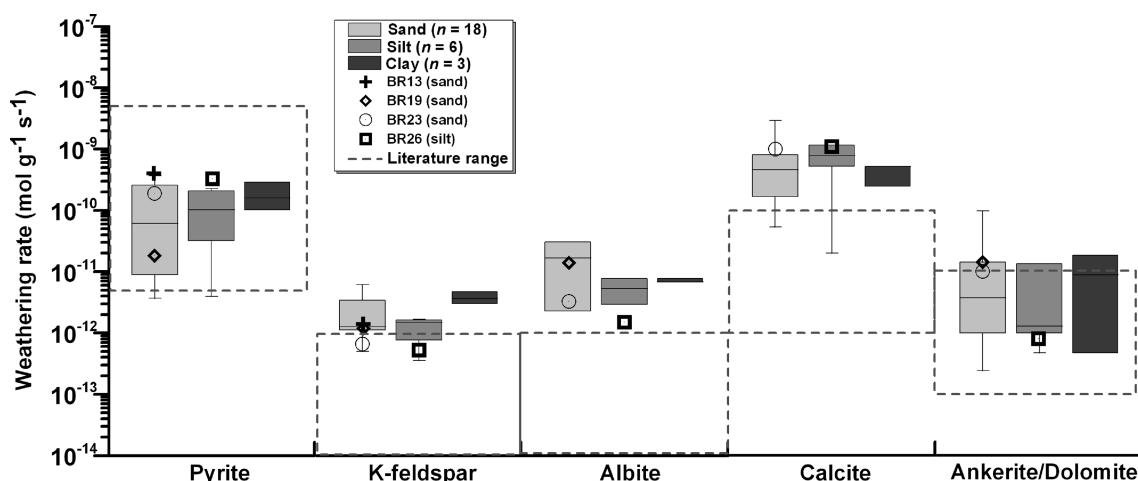


FIGURE 5. Weathering rates ($\text{mol g}^{-1}_{\text{mineral}} \text{s}^{-1}$) from nonsacrificial (box plots) versus sacrificial experiments (symbols) for kinetic mineral reactions. Reported weathering rates (dashed boxes) compiled from refs 10, 25, 33, 36, and 37.

ferences in weathering estimates; dissolution rates for K-feldspar and plagioclase were similar (36, 37), and calcite weathering rates were faster than ankerite rates by at least one order-of-magnitude (25). Overall, the weathering rates for the sacrificial experiments were within the range obtained for the nontemporal experiments, indicating the ability to extrapolate this approach.

Implications for Field-Scale Modeling of Heterogeneous Aquifers. The combined experimental and kinetic modeling approach provided a robust method for interpreting reductant behavior and to quantify reaction rates and their variability for competing oxidation and buffering reactions in different lithologies. The overall assessment was constrained by an extensive data set including gas-phase evolution and aqueous compositional changes that allowed elucidate the reactivity of competing reductants and their relative contributions to oxidant consumption. Thereby, modeling acted as a unifying framework enabling a comprehensive process-based explanation for the variability in the observed geochemical responses during sediment incubations. It was found that concentration-normalized mineral reaction rates were similar across the different lithologies. Pyrite was most abundant in the finer grained material, and therefore corresponding reaction rates were highest. Pyrite oxidation was found to significantly enhance the aluminosilicate and carbonate dissolution rates independent of the lithology.

The model derived (A/V) parameters and rate constants for the studied aquifer sequence can be scaled to the in situ pore volume but should be used with caution. Differing experimental conditions only allow them to be considered as best initial estimates for field-scale reactive transport modeling. For instance diffusive limitations of reaction rates were suppressed by the continuous stirring of the sediment suspension during the experiments, and therefore the calibrated (A/V) parameters and rate constants reflect upper limits. However, the relative differences in mineral reaction rates identified for the different lithologies are expected to persist under field conditions.

The combined experimental and modeling approach presented in this study can therefore be utilized to underpin the construction of numerical models describing reactive transport in physically and geochemically heterogeneous aquifers.

Acknowledgments

This research was funded by the Water Foundation and Water Corporation of Western Australia. C.D. acknowledges assistance from Water for a Healthy Country Flagship (CSIRO),

Schlumberger Water Services, F.S. Shaw Memorial, and CONICYT. We gratefully acknowledge Linn Wilfert's help with the experiments. We thank Anna Kaksonen, Evelien Martens, and three anonymous reviewers' comments that helped improve the manuscript.

Supporting Information Available

Additional information on the study site, analytical methods, SEM images, the setup and definition of the numerical model, and simulation results for the nonsacrificial experiments. This material is available free of charge via the Internet at <http://pubs.acs.org>.

Literature Cited

- Landmeyer, J. E.; Chapelle, F. H.; Herlong, H. H.; Bradley, P. M. Methyl tert-butyl ether biodegradation by indigenous aquifer microorganisms under natural and artificial oxic conditions. *Environ. Sci. Technol.* **2001**, 35 (6), 1118–1126.
- Lee, K.; Mora, S. D. In situ bioremediation strategies for oiled shoreline environments. *Environ. Technol.* **1999**, 20 (8), 783–794.
- Seidel, D. C. Extracting uranium from its ores. *IAEA Bull.* **1981**, 23 (2), 24–28.
- Prommer, H.; Stuyfzand, P. J. Identification of temperature-dependent water quality changes during a deep well injection experiment in a pyritic aquifer. *Environ. Sci. Technol.* **2005**, 39 (7), 2200–2209.
- Greskowiak, J.; Prommer, H.; Vanderzalm, J.; Pavelic, P.; Dillon, P. Modeling of carbon cycling and biogeochemical changes during injection and recovery of reclaimed water at Bolivar, South Australia. *Water Resour. Res.* **2005**, 41 (10), 16.
- Mansell, J.; Drewes, J. E. Fate of steroid hormones during soil-aquifer treatment. *Ground Water Monit. Remediat.* **2004**, 24, 94–101.
- Greskowiak, J.; Prommer, H.; Massmann, G.; Nuttmann, G. Modeling seasonal redox dynamics and the corresponding fate of the pharmaceutical residue phenazone during artificial recharge of groundwater. *Environ. Sci. Technol.* **2006**, 40 (21), 6615–6621.
- Descourvières, C.; Hartog, N.; Patterson, B. M.; Oldham, C.; Prommer, H. Geochemical controls on sediment reactivity and buffering processes in a heterogeneous aquifer. *Appl. Geochem.* **2010**, 25 (2), 261–275.
- Postma, D.; Boesen, C.; Kristiansen, H.; Larsen, F. Nitrate Reduction in an Unconfined Sandy Aquifer - Water Chemistry, Reduction Processes, and Geochemical Modeling. *Water Resour. Res.* **1991**, 27 (8), 2027–2045.
- Williamson, M. A.; Rimstidt, J. D. The Kinetics and Electrochemical Rate-Determining Step of Aqueous Pyrite Oxidation. *Geochim. Cosmochim. Acta* **1994**, 58 (24), 5443–5454.
- Moses, C. O.; Herman, J. S. Pyrite oxidation at circumneutral pH. *Geochim. Cosmochim. Acta* **1991**, 55 (2), 471–482.

- (12) Elberling, B.; Nicholson, R. V. Field determination of sulphide oxidation rates in mine tailings. *Water Resour. Res.* **1996**, 32 (6), 1773–1784.
- (13) Fennemore, G. G.; Neller, W. C.; Davis, A. Modeling pyrite oxidation in arid environments. *Environ. Sci. Technol.* **1998**, 32 (18), 2680–2687.
- (14) Andersen, M. S.; Larsen, F.; Postma, D. Pyrite oxidation in unsaturated aquifer sediments. Reaction stoichiometry and rate of oxidation. *Environ. Sci. Technol.* **2001**, 35 (20), 4074–4079.
- (15) Barcelona, M. J.; Holm, T. R. Oxidation-reduction capacities of aquifer solids. *Environ. Sci. Technol.* **1991**, 25 (9), 1565–1572.
- (16) Vacher, H. L.; Hutchings, W. C.; Budd, D. A. Metaphors and models: The ASR bubble in the Floridan aquifer. *Ground Water* **2006**, 44 (2), 144–154.
- (17) Dagan, G. Solute transport in heterogeneous porous formations. *J. Fluid Mech.* **1984**, 145, 151–77.
- (18) Allen-King, R. M.; Halket, R. M.; Gaylord, D. R.; Robin, M. J. L. Characterizing the heterogeneity and correlation of perchloroethene sorption and hydraulic conductivity using a facies-based approach. *Water Resour. Res.* **1998**, 34 (3), 385–396.
- (19) Scheibe, T. D.; Fang, Y. L.; Murray, C. J.; Roden, E. E.; Chen, J. S.; Chien, Y. J.; Brooks, S. C.; Hubbard, S. S. Transport and biogeochemical reaction of metals in a physically and chemically heterogeneous aquifer. *Geosphere* **2006**, 2 (4), 220–235.
- (20) Parkhurst, D. L.; Appelo, C. A. J. User's guide to PHREEQC (Version 2) -- A computer program for speciation, reaction-path, advective-transport and inverse geochemical calculations; U.S. Geological Survey: Reston, VA, 1999.
- (21) Mayer, K.; Frind, E.; Blowes, D. Multicomponent reactive transport modeling in variably saturated porous media using a generalized formulation for kinetically controlled reactions. *Water Resour. Res.* **2002**, 38 (9), 1174.
- (22) Eckert, P.; Appelo, C. A. J. Hydrogeochemical modeling of enhanced benzene, toluene, ethylbenzene, xylene (BTEX) remediation with nitrate. *Water Resour. Res.* **2002**, 38 (8), 1130.
- (23) Appelo, C. A. J.; Postma, D. *Geochemistry, groundwater and pollution*, 2nd ed.; A.A. Balkema Publishers: Amsterdam, The Netherlands, 2005.
- (24) Plummer, L. N.; Wigley, T. M. L.; Parkhurst, D. L. The kinetics of calcite dissolution in CO₂-water systems at 5° to 60 °C and 0. 0 to 1. 0 atm CO₂. *Am. J. Sci.* **1978**, 278, 179–216.
- (25) Chou, L. E. I.; Garrels, R. M.; Wollast, R. Comparative study of the kinetics and mechanisms of dissolution of carbonate minerals. *Chem. Geol.* **1989**, 78 (3–4), 269–282.
- (26) Watson, M. Petrological characterisation of the Vlaming Sub-Basin, Perth Basin for the purpose of CO₂ storage; CO₂CRC Publication Number RPT06-0098: 2006.
- (27) Al, T. A.; Martin, C. J.; Blowes, D. W. Carbonate-mineral/water interactions in sulfide-rich mine tailings. *Geochim. Cosmochim. Acta* **2000**, 64 (23), 3933–3948.
- (28) Busenberg, E.; Plummer, L. N. The kinetics of dissolution of dolomite in CO₂-H₂O systems at 1.5 to 65 °C and 0 to 1 atm PCO₂. *Am. J. Sci.* **1982**, 282 (1), 45–78.
- (29) Sverdrup, H.; Warfvinge, P. Estimating field weathering rates using laboratory kinetics. *Rev. Mineral. Geochem.* **1995**, 31 (1), 485–541.
- (30) Rimstidt, J. D.; Barnes, H. L. The kinetics of silica-water reactions. *Geochim. Cosmochim. Acta* **1980**, 44, 1683–1699.
- (31) Dzombak, D. A.; Morel, F. M. M. *Surface Complexation Modeling: Hydrous Ferric Oxide*; Wiley-Interscience: New York, 1990.
- (32) Doherty, J. *PEST Model-Independent Parameter Estimation User Manual*; Watermark Numerical Computing: Brisbane, Australia, 2004.
- (33) Nicholson, R. V.; Gillham, R. W.; Reardon, E. J. Pyrite oxidation in carbonate-buffered solution: 1. Experimental kinetics. *Geochim. Cosmochim. Acta* **1988**, 52 (5), 1077–1085.
- (34) Appelo, C. A. J.; Verweij, E.; Schafer, H. A hydrogeochemical transport model for an oxidation experiment with pyrite/calcite/exchangers/organic matter containing sand. *Appl. Geochem.* **1998**, 13 (2), 257–268.
- (35) Walter, L.; Morse, J. Reactive surface area of skeletal carbonates during dissolution--effect of grain size. *J. Sediment. Petrol.* **1984**, 54 (4), 1081–90.
- (36) Knauss, K. G.; Wolery, T. J. Dependence of albite dissolution kinetics on pH and time at 25 and 70 °C. *Geochim. Cosmochim. Acta* **1986**, 50 (11), 2481–2497.
- (37) White, A. F.; Brantley, S. L. Chemical weathering rates of silicate minerals: an overview. In *Chemical weathering rates of silicate minerals. Reviews in Mineralogy*; White, A. F., Brantley, S. L., Eds.; Washington, DC, 1995; Vol. 31, pp 1–22.

ES101661U